Experimental Investigation of the Ce-Mg-Mn Isothermal Section at 723 K (450 °C) *via* Diffusion Couples Technique

AHMAD O. MOSTAFA and MAMOUN MEDRAJ

The isothermal section of the Ce-Mg-Mn phase diagram at 723 K (450 °C) was established experimentally by means of diffusion couples and key alloys. The phase relationships in the complete composition range were determined based on six solid–solid diffusion couples and twelve annealed key alloys. No ternary compounds were found in the Ce-Mg-Mn system at 723 K (450 °C). X-ray diffraction and energy-dispersive X-ray spectroscopy spot analyses were used for phase identification. EDS line-scans, across the diffusion layers, were performed to determine the binary and ternary homogeneity ranges. Mn was observed in the diffusion couples and key alloys microstructures as either a solute element in the Ce-Mg compounds or as a pure element, because it has no tendency to form intermetallic compounds with either Ce or Mg. The fast at. interdiffusion of Ce and Mg produces several binary compounds (Ce_xMg_y) during the diffusion process. Thus, the diffusion layers formed in the ternary diffusion couples were similar to those in the Ce-Mg binary diffusion couples, except that the ternary diffusion couples contain layers of Ce-Mg compounds that dissolve certain amount of Mn. Also, the ternary diffusion couples showed layers containing islands of pure Mn distributed in most diffusion zones. As a result, the phase boundary lines were pointing toward Mn-rich corner, which supports the tendency of Mn to be in equilibrium with all the phases in the system.

DOI: 10.1007/s11661-014-2251-z

I. INTRODUCTION

MAGNESIUM alloys are in increasing demand because of their unique properties. Some of the major advantages of magnesium alloys are: lowest density among all other metallic structural materials, high specific strength, good castability, suitability for high-pressure die casting, high speed machinability, good weldability under controlled atmosphere, availability,[1] and improved corrosion resistibility against salty water compared to pure Mg.[2] To obtain these advantages, attempts have been made to improve the mechanical properties of Mg by adding different alloying elements. For instance, addition of cerium leads to improved mechanical properties at elevated temperatures.[3] Furthermore, addition of manganese improves the corrosion resistance.[4] Ce-Mg-Mn alloys are considered promising for automotive and aerospace applications. They show excellent creep resistance at elevated temperatures.[1] Their light weight, also, gives an opportunity for further structural weight reduction. Thus, it is essential to understand the phase relationships, resulting from addition of Ce and Mn to Mg, in the Ce-Mg-Mn system using different techniques.

The diffusion couple is a valuable experimental technique for phase diagram studies. It is subjected to the assumption of obtaining local equilibria in the diffusion zones.[5] Thin layers, in thermodynamic equilibrium, are formed adjacent to each other. The phase equilibria, then, can be determined *via* the composition profiles across these layers.[6]

II. LITERATURE DATA

A. *The Ce-Mn System*

The Ce-Mn phase diagram was studied experimentally by several investigators.[7–11] Rolla and Iandelli[7] and Iandelli[8] first suggested that a liquid miscibility gap exists at 1271 K (998 °C) in the composition range of 45 to 64 wt pct Mn. Later, Thamer[9] investigated the Ce-Mn system in the Ce-rich side (below 20 at. pct Mn). He[9] found that the eutectic occurs at 895 K (622 °C), which is 10 K (−263 °C) higher than the eutectic temperature proposed by Iandelli[8] at 885 K (612 °C). Also, he[9] reported the solubility of Mn as 5 at. pct in δ-Ce and 2 at. pct in γ-Ce at 911 K (638 °C). Palenzona and Cirafici[10] re-assessed the Ce-Mn phase diagram experimentally, taking into account all previous thermal analyses reported by Thamer.[9] They[10] corrected the allotropic transition temperatures of $\alpha \rightarrow \beta$ Mn to 1000 K (727 °C) instead of 983 K (710 °C), $\beta \rightarrow \gamma$ to 1373 K (1100 °C) instead of 1343 K (1070 °C), and $\gamma \rightarrow \delta$ to 1411 K (1138 °C) instead of 1416 K (1143 °C). The melting temperature of Mn remained the same as 1519 K (1246 °C). Because of the presence of the liquid miscibility gap in the Ce-Mn phase diagram, Tang *et al.*[11] re-assessed the system based on their own

AHMAD O. MOSTAFA, Ph.D. Student, and MAMOUN MEDRAJ, Professor of Materials Engineering, are with the Mechanical and Industrial Engineering Department, Concordia University, 1455 de Maisonneuve Blvd West, Montreal, QC H3G 1M8, Canada. Contact e-mail: mmedraj@encs.concordia.ca
Manuscript submitted June 29, 2013.

Published online: 06 March 2014

XRD and DTA measurements and the data from the literature.[8,9] Furthermore, the Ce-Mn system was thermodynamically modeled by Tang *et al.*[12] and Kang *et al.*[13] considering all the experimental findings, except the liquid miscibility gap proposed by Iandelli.[8]

B. *The Mg-Mn System*

Several experimental works[14–17] and thermodynamic modeling[13,17,18] concerning the binary Mg-Mn phase diagram were found in the literature. However, due to the high temperature of the liquid miscibility gap, experimental data are not available in this region. The temperature was estimated, using thermodynamic modeling, by many authors as 2175 K (1902 °C),[13] 3475 K (3202 °C),[17] and 3688 K (3415 °C).[18] The binary liquid miscibility gap, of the Mg-Mn binary system, was proposed to extend in the Ce-Mg-Mn ternary, based on the liquidus projection calculated by Zhang *et al.*[19]

C. *The Ce-Mg System*

Unlike the other two binaries, intermetallic compounds exist in the Ce-Mg system. The Ce-Mg phase diagram was experimentally studied by many authors.[20–24] Accordingly, Figure 1 shows the Ce-Mg phase diagram redrawn from Nayeb-Hashemi and Clark.[25] Recently, Zhang *et al.*[26] reported a shift in the compositions of Ce_5Mg_{41} and $CeMg_{12}$. Based on their[26] findings, some compounds were given different formulae such as Ce_5Mg_{39} instead of Ce_5Mg_{41} and $CeMg_{11}$ instead of $CeMg_{12}$. These compositional shifts were due to substitution of Mg sites with vacancies.

More recently, Okamoto[27] re-evaluated the Ce-Mg phase diagram focusing on the modified phase diagram by Zhang *et al.*[26,28,29] Based on the crystal structure data, Okamoto[27] changed Ce_5Mg_{39} and $CeMg_{11}$ to their former formulae Ce_5Mg_{41} and $CeMg_{12}$, respectively. Table I shows the crystal structure data and actual composition of Ce-Mg compounds.[27,30] Also, he[27] suggested the re-examination of the $CeMg_3$ phase field; since the width of the two-phase region $CeMg_2 + CeMg_3$ was shown to increase with temperature.

D. *The Ce-Mg-Mn System*

The Ce-Mg-Mn ternary system was first studied by Petrov *et al.*[3] The samples were prepared initially from Mg-Mn master alloys containing 2.5 wt pct Mn. They[3] reported two vertical sections in the Mg-rich corner, at maximum 3 wt pct Mn with 0.3 and 1.6 wt pct Ce, respectively, by thermal and microscopic methods. No ternary compounds were observed in the two vertical sections. Based on the results of Petrov *et al.*,[3] Raynor[31] concluded that addition of 1.5 wt pct Ce to Mg-Mn alloys reduces the solid solubility of Mn from 5 to 3.8 wt pct at 1123 K (850 °C), while further additions will slightly affect the Mn solubility. Later, the Ce-Mg-Mn ternary system was studied by Pezat *et al.*[32] They attempted partial substitution of Mg by M = (V, Cr, Mn, Fe, and Co) in $CeMg_{12}$ to investigate the $CeMg_{11}M$ composition as a hydrogen storage compound. In their findings, $CeMg_{11}Mn$ was reported as a ternary compound. After further examination, they realized that $CeMg_{11}M$ was only a chemical composition in the $CeMg_{12}$ + Mn two-phase field and not a ternary compound. Recently, Zhang *et al.*[19] studied the Mg-rich corner (up to 2.5 wt pct Mn and 25 wt pct Ce) of the Ce-Mg-Mn phase diagram experimentally with the aid of thermodynamic modeling. High-purity starting materials were used in their[19] work and three isopleths at 0.6, 1.8, and 2.5 wt pct Mn and Ce up to 25 wt pct were selected. The system was investigated using two thermal analysis methods [cooling curve analysis (CCA) and DSC], SEM/EPMA and XRD techniques. A ternary eutectic reaction was observed at the composition of 1 wt pct Mn and 23 wt pct Ce and temperature of 865 K (592 °C). In addition, the homogeneity range of $CeMg_{12}$ varies between 0.3 at. pct and 0.6 at. pct Mn, depending on alloy composition. Zhang *et al.*[19] also mentioned that $Ce(Mg,Mn)_{12}$ ternary solid solution has the same tetragonal structure as $CeMg_{12}$, indicating the substitution of Mg by Mn. No additional experimental data could be found on this system in the literature.

The main objective of this work is to establish the Ce-Mg-Mn isothermal section at 723 K (450 °C) experimentally by means of diffusion couples and key alloys. This will give better understanding of the phase relationships in the system, which is necessary for alloy design and development.

III. EXPERIMENTAL PROCEDURE

In order to study the phase relationships in the Ce-Mg-Mn isothermal section at 723 K (450 °C), six solid–solid diffusion couples along with twelve key alloys were prepared and analyzed using Hitachi S-3400 scanning electron microscope equipped with energy-dispersive X-ray spectrometer (SEM/EDS). In most cases, the solubility ranges extended from the Ce-Mg binary compounds were below the detection limit of the EDS detector. Thus, the EDS results were used for qualitative analysis and the small solubilities were indicated as less than 2 at. pct. X-ray diffraction was performed on powdered samples, in the range from 20 to 90 deg 2θ with 0.02 deg step size, to identify and confirm the phases obtained by EDS measurements. X-ray phase analysis was carried out using X'pert Highscore Plus software.[33] The standard intensity data were taken from Pearson's Crystal Data software.[30] Silicon was used in the powder samples as a calibration standard to correct for the zero shift and specimen displacement.

A. *Key Alloys Preparation*

Pure elements were used for alloy preparation and diffusion couple end-members. Ce ingots and Mn flakes with purity of 99.9 and 99.98 pct, respectively, were supplied by Alfa Aesar Co.; and Mg ingots with purity of 99.8 pct were supplied by CANMET Materials Technology Laboratory (CANMET-MTL). The key alloys were prepared in an arc-melting furnace with water-cooled copper crucible and a non-consumable

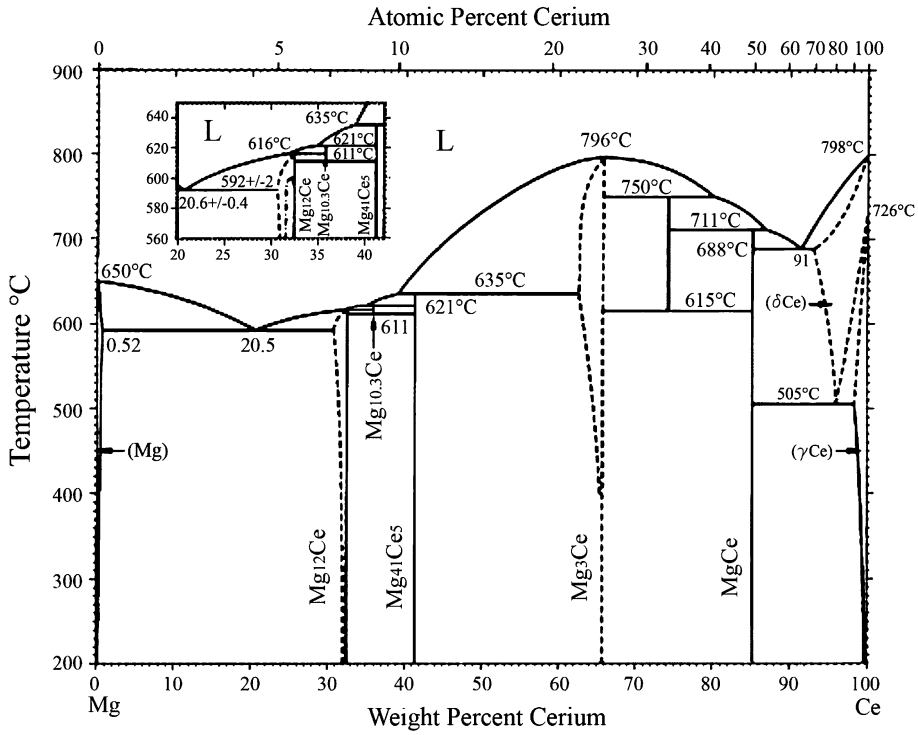

Fig. 1—The Ce-Mg phase diagram redrawn from Nayeb-Hashemi and Clark.[25]

Table I. Crystal Structure Data and Actual Composition of Ce-Mg Compounds[27,30]

Phase	Composition, at. pct Mg	Pearson's Symbol	Space Group	Structure Type	Lattice Parameters (Å)	
					a	*c*
(δCe)	0 to 30	*cI2*	*Im3m*	W	4.120	
(γCe)	0 to 8.2	*cF4*	*Fm3m*	Cu	5.160	
CeMg	50	*cP2*	*Pm3m*	CsCl	3.901	
$CeMg_2$	66.7	*cF24*	*Fd3m*	Cu_2Mg	8.733	
$CeMg_3$	74.7 to 77	*cF16*	*Fm3m*	BiF_3	7.420	
Ce_5Mg_{41}	89.1	*tI92*	*I4/m*	Ce_5Mg_{41}	14.540	10.280
$CeMg_{10.3}$	91.2	*hP38*	$P6_3/mmc$	$Ni_{17}Th_2$	10.350	10.260
$CeMg_{12}$	92.5 to 93	*tI26*	*I4/mmm*	$Mn_{12}Th$	10.330	5.960
Mg	100	*hP2*	$P6_3/mmc$	Mg	3.207	5.210

tungsten electrode under argon. The alloys were melted several times to ensure the composition homogeneity. Excess amount of Mg (around 15 pct) was added to compensate for Mg losses due to evaporation. The actual global composition was determined using an Ultima2 inductively coupled plasma optical emission spectrometry (ICP-OES). The actual composition was determined by taking the average composition of three different portions from each sample.

B. *Solid–Solid Diffusion Couples*

The end-members of the solid–solid diffusion couples were prepared from pure metals and/or alloys. Table II shows the compositions of the end-members and the annealing time periods of the diffusion couples annealed at 723 K (450 °C). The contacting surfaces were ground gradually up to 1200 SiC paper using 99 pct pure ethanol as a lubricant and to prevent oxidation. High friction between the samples and the SiC papers was avoided to eliminate sparking during grinding due to Ce. After that, the ground surfaces were polished down to 1 μm using alcohol diamond suspension. The end-members were strongly tightened together using stainless steel clamping rings to ensure good surface contact between the two members.

For annealing purposes, alloys and diffusion couples were wrapped in tantalum foil and encapsulated inside an argon-purged quartz tube with the inside pressure of about 5×10^{-1} torr. To reach equilibrium at 723 K (450 °C), alloys were heated up to 773 K (500 °C) for 1 hour, and then the furnace temperature was brought down to 723 K (450 °C) and kept for different annealing time. Therefore, annealing time was chosen as 8 days for some compositions, since no complete phase equilibrium was obtained from preliminary annealing attempts for 4

Table II. Composition and Annealing Conditions of the Diffusion Couples

Couple	First End-Member (at. pct)			Second End-Member (at. pct)			Time (days)	Temperature [K (°C)]
	Ce	Mg	Mn	Ce	Mg	Mn		
#1	52.6	19.8	27.6	—	100	—	8	723 (450)
#2	34.7	38.1	27.2	—	100	—	8	723 (450)
#3	7.0	87.4	5.6	100	—	—	6	723 (450)
#4	60.0	40.0	—	—	—	100	10	723 (450)
#5	34.4	38.1	27.2	100	—	—	5	723 (450)
#6	52.6	19.8	27.6	14.5	82.7	2.8	4	723 (450)

days. Other alloys were annealed for 35 days; especially those containing $CeMg_2$ phase. This was due to the slow kinetics of the eutectoidal decomposition of the $CeMg_2$ into (CeMg) and ($CeMg_3$). The diffusion couples were annealed at 723 K (450 °C) for different periods of time, based on the composition of the chosen end-members. The annealing process was stopped when the tube was visually observed to be dark indicating significant evaporation. After annealing, the quartz tubes, containing alloys and diffusion couples, were rapidly quenched in cold water in order to maintain the high temperature structure. The equilibrated phases and the diffusion zones were analyzed using SEM/EDS spot analysis and line-scans. Based on the phase equilibrium data obtained from six solid–solid diffusion couples and 12 key alloys, the isothermal section of the Ce-Mg-Mn phase diagram at 723 K (450 °C) was constructed.

IV. RESULTS AND DISCUSSION

Diffusion couple technique combined with selected equilibrated alloys is used to achieve more reliable equilibrium phase relations in the Ce-Mg-Mn system. This combination guarantees the accuracy of the obtained data. In this work, six solid–solid diffusion couples were prepared and studied. Among these couples, only #1, #3, #4, and #6 will be presented in details. Diffusion couples #2 and #5 will not be discussed because diffusion couple #2 showed similar results to diffusion couple #1, and diffusion couple #5 confirmed the results obtained from other diffusion couples.

In the following section, the binary solid solution of Mg in γCe is represented as $(\gamma Ce)^{Mg}$, and the extended solid solubility of Mg and Mn in γCe is represented as $(\gamma Ce)^{Mg,Mn}$. Also, the details of the equilibrium information obtained from the samples used in the diffusion couples end-members are covered in the key alloys part (Section IV–B).

A. *Diffusion Couples*

The SEM micrograph of diffusion couple #1 is presented in Figures 2(a), (b) and (c). The first end-member was made from pure Mg. The second end-member was made from sample #2, containing three phases, $(\gamma Ce)^{Mg,Mn}$, (CeMg), and Mn, as shown in Figure 2(d). Six diffusion zones were observed after annealing at 723 K (450 °C) for 8 days. EDS spot analysis was carried out to measure the composition of each zone. The EDS line-scan, shown in Figure 3, was performed across the diffusion zones of diffusion couple #1 to measure the homogeneity ranges of the different phases. The EDS spot analysis and line-scan results of diffusion couple #1 are summarized in Table III. It can be seen from the composition of the phases of diffusion couple #1 that Mn was associated with every diffusion zone as a pure element. Mn was originally provided from sample #2 (end-member). During the annealing process, adjacent layers representing the Ce-Mg binary compounds started to form, due to the fast atomic interdiffusion between Ce and Mg atoms. Mn was filtered from the end-member alloy, because it did not react with the diffusing components. This could be an indication that Mn is in equilibrium with these phases. Thus, four two-phase equilibria, namely ($CeMg_{12}$) + Mn, Ce_5Mg_{41} + Mn, ($CeMg_3$) + Mn, and (CeMg) + Mn were observed within the diffusion layers of couple #1; whereas, three three-phase equilibria were found at the interfaces. These three-phase equilibria are ($CeMg_{12}$) + Mn + Ce_5Mg_{41}, Ce_5Mg_{41} + Mn + ($CeMg_3$), and ($CeMg_3$) + Mn + (CeMg). The Ce-Mg binary phase diagram[25] showed CeMg as a stoichiometric compound. However, the ternary results showed (CeMg) as a solid solution with 2.5 at. pct Mn (Table III). Thus, (CeMg) was used to describe this extended solid solution.

SEM micrographs of diffusion couple #1 showed that Mn was not contributing to the diffusion process, because Mn was localized in all diffusion zones as a pure element. Nevertheless, a continuous very thin layer of pure Mn was observed near the Mg end-member, as shown in Figure 2(c). This layer indicates that Mn was also diffusing during the diffusion process. The diffusing Mn is in the form of small particles that most probably resulted from the dissolution of the $(\gamma Ce)^{Mg,Mn}$ solid solution present in the end-member. The existence of Mn layer between Mg and ($CeMg_{12}$) + Mn two-phase field is necessary to fulfill the phase equilibrium. The Mn layer was not completely shown in the composition profile (Figure 3), because the layer thickness was much smaller than the spatial displacement of the point-to-point line-scan, which is ~1 μm in average.

Based on the microstructures of the diffusion zones and the composition profiles, the diffusion path can

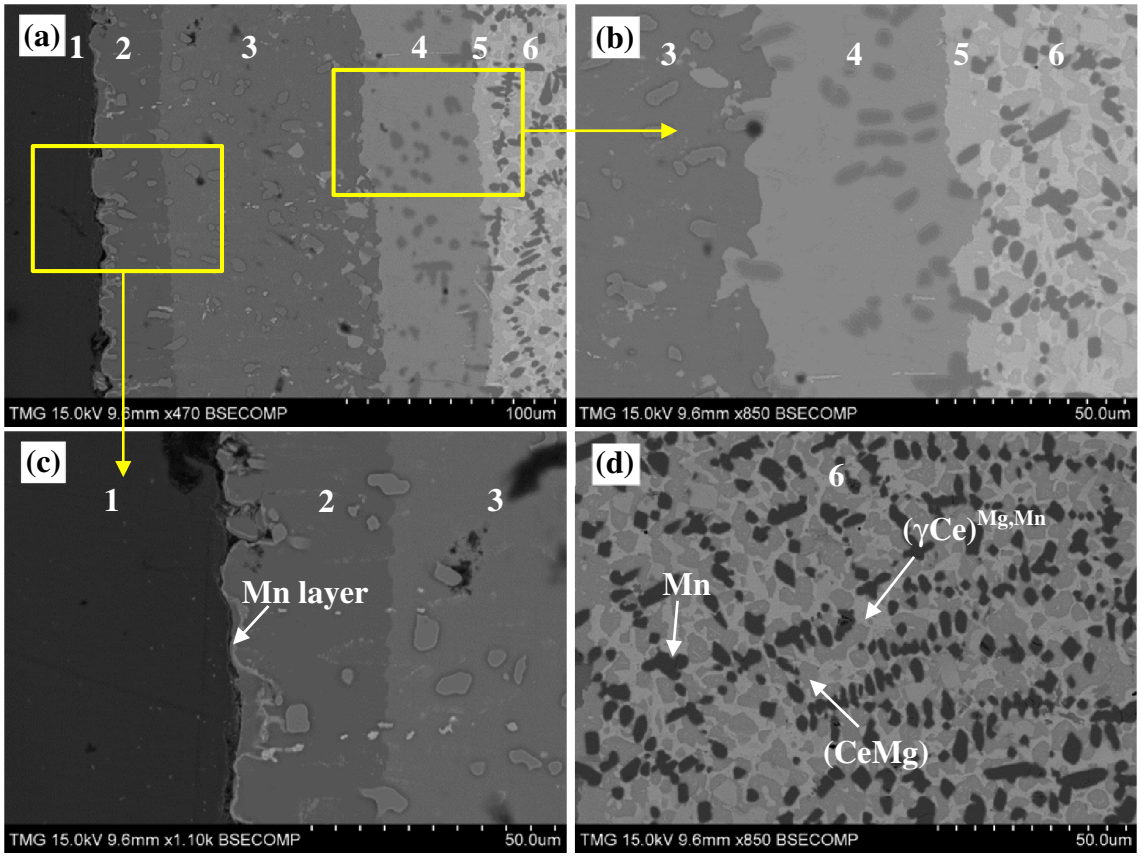

Fig. 2—(*a–c*) SEM micrographs of the diffusion zones of diffusion couple #1; (*d*) microstructure of sample #2 (52.6Ce-19.8Mg-27.6Mn at. pct). The numbers represent the diffusion zones and correspond to those in Fig. 3 and Table III.

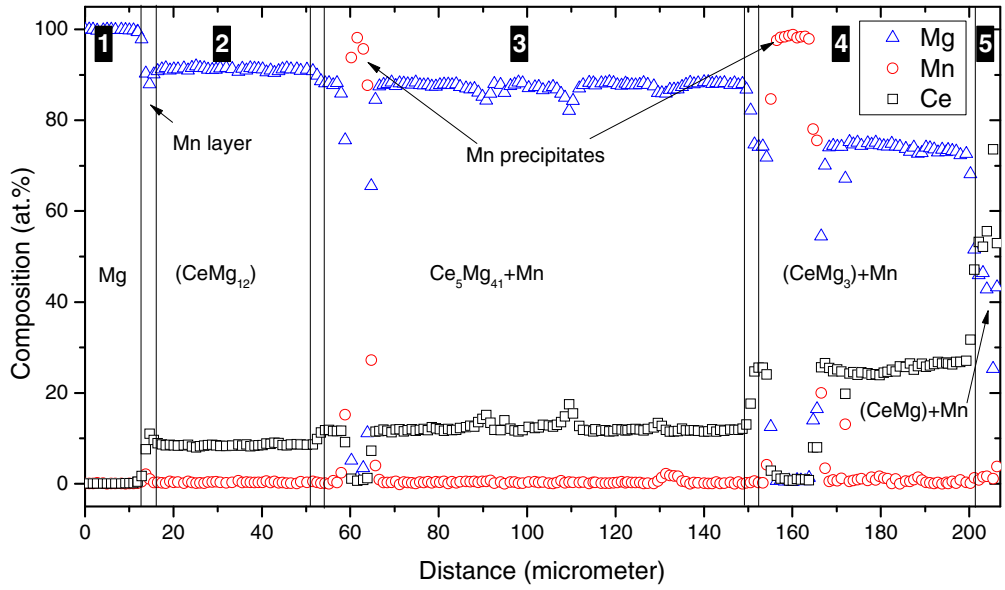

Fig. 3—Composition profile obtained by EDS line-scan across diffusion zones of the diffusion couple #1.

be depicted as follows: $(\gamma Ce)^{Mg,Mn}$ + (CeMg) + Mn (end-member) → (CeMg) + Mn → $(CeMg_3)$ + Mn + (CeMg) → $(CeMg_3)$ + Mn → Ce_5Mg_{41} + Mn + $(CeMg_3)$ → Ce_5Mg_{41} + Mn → $(CeMg_{12})$ + Mn + Ce_5Mg_{41} → $(CeMg_{12})$ + Mn → pure Mn → pure Mg (end-member). The arrows used here indicate the phase boundary lines and not a chemical reaction. The phase equilibria obtained from diffusion couple #1 are represented graphically in Figure 4. The two end-members of diffusion couple #1 are connected by a dashed line.

Table III. Phases Composition Obtained by EDS Spot Analysis and Line-Scan of Diffusion Couple #1

Zone	Description	Composition (at. pct) Ce	Mg	Mn	Corresponding Phase
1	pure Mg (end-member)	0	100	0	Mg
2	two-phase layer	8.5	91.5	0	$(CeMg_{12})$
		0	0	100	Mn
3	three-phase layer	11.8	88.2	0	Ce_5Mg_{41}
		0	100	0	Mn
		24.6	74.7	<2.0	$(CeMg_3)$
4	two-phase layer	24.6 to 26.7	73.1 to 74.7	<2.0	$(CeMg_3)$
		0	0	100	Mn
5	two-phase layer	48.0	51.5	<2.0	(CeMg)
		0	0	100	Mn
6	three-phase alloy	53.9	43.5	2.6	(CeMg)
	sample #2 (end-member)	95.6	3.7	<2.0	$(\gamma Ce)^{Mg,Mn}$
		0	0	100	Mn

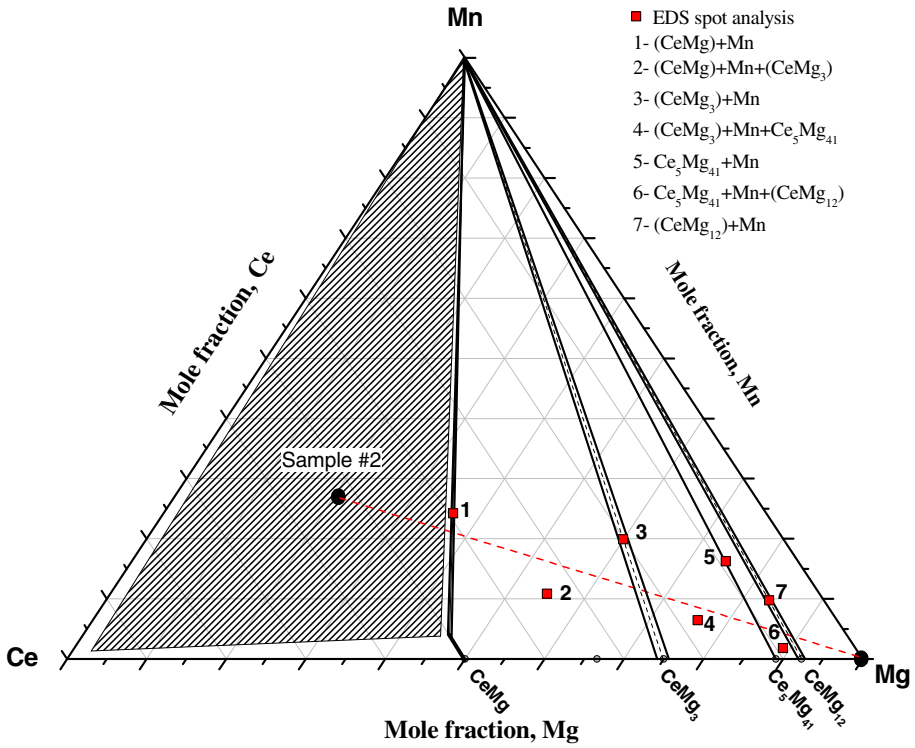

Fig. 4—Phase equilibria depicted from diffusion couple #1.

The shaded triangle in Figure 4 represents the three-phase equilibria of sample #2. Points 1, 3, 5, and 7 represent the two-phase equilibria between Mn and (CeMg), $(CeMg_3)$, Ce_5Mg_{41}, and $(CeMg_{12})$, respectively; whereas points 2, 4, and 6 represent the three-phase equilibria (CeMg) + Mn + $(CeMg_3)$, $(CeMg_3)$ + Mn + Ce_5Mg_{41}, and Ce_5Mg_{41} + Mn + $(CeMg_{12})$, respectively.

Diffusion couple #1 revealed the phase relationships from 0 to 50 at. pct Ce in the Ce-Mg-Mn phase diagram at 723 K (450 °C), which normally requires large no. of key alloys to provide the same results. The results of diffusion couple #1 were confirmed by the results of diffusion couple #2, because the composition of their end-members is in close proximity.

The SEM micrograph of diffusion couple #3 is presented in Figure 5(a). Figure 5(b) shows the SEM micrograph of the end-member which was made from the $(CeMg_{12})$ + Mn two-phase alloy (sample #8). The other end-member was made from a block of pure Ce. After annealing and quenching, seven diffusion zones were observed. EDS line-scan was performed across the diffusion zones to determine the homogeneity ranges of

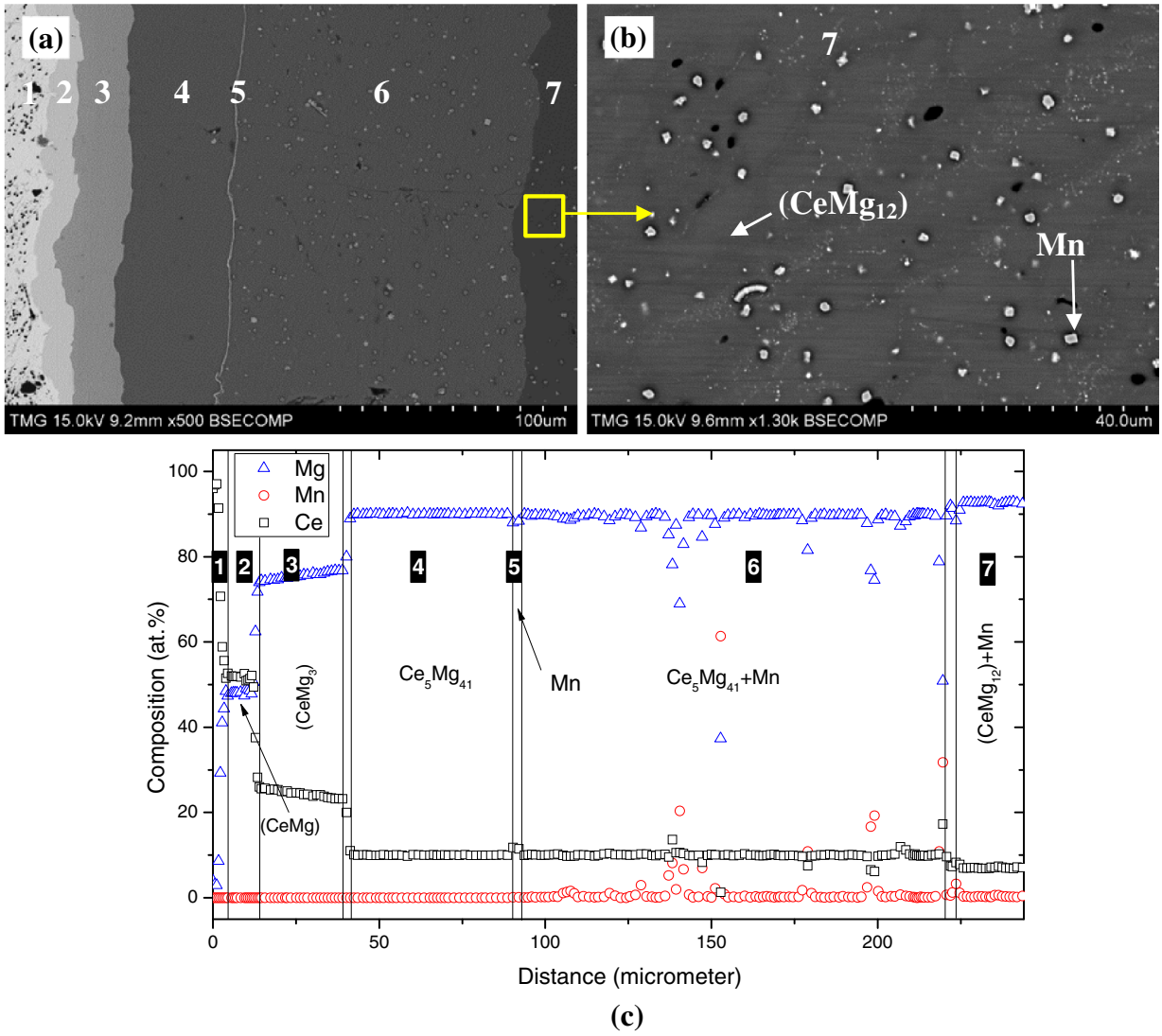

Fig. 5—(*a*) SEM micrograph of diffusion couple #3; (*b*) SEM micrograph of sample #8; (*c*) EDS line-scan across the diffusion zones of diffusion couple #3. The numbers represent the diffusion zones and correspond to those in Table IV.

Table IV. Phases Composition Obtained by EDS Spot Analysis and Line-Scan of Diffusion Couple #3

Zone	Description	Composition (at. pct)			Corresponding Phase
		Ce	Mg	Mn	
1	pure Ce (end-member)	100	0	0	Ce
2	single-phase layer	51.0 to 52.5	47.5 to 49.0	0	(CeMg)
3	single-phase layer	23.3 to 25.6	74.4 to 76.7	0	($CeMg_3$)
4	single-phase layer	10.9	89.1	0	Ce_5Mg_{41}
5	single-phase layer	0	0	100	Mn
6	two-phase layer	10.9	89.1	0	Ce_5Mg_{41}
		0	0	100	Mn
7	two-phase alloy	8.0	91.7	<1.0	($CeMg_{12}$)
	sample #8 (end-member)	0	0	100	Mn

the phases within the diffusion zones. The composition of the phases of each diffusion zone is given in Table IV.

The ternary diffusion couple #3 behaved like Ce-Mg binary diffusion couple, where only binary phases formed until the end of zone #4. These phases, starting from Ce side, are CeMg, $CeMg_3$, and Ce_5Mg_{41}. Ce_5Mg_{41} seems to be in equilibrium with Mn, since a continuous thin layer of pure Mn (zone #5), similar to that in diffusion couple #1, formed at the interface between zones #4 and #6 as shown in Figure 5(a). Mn

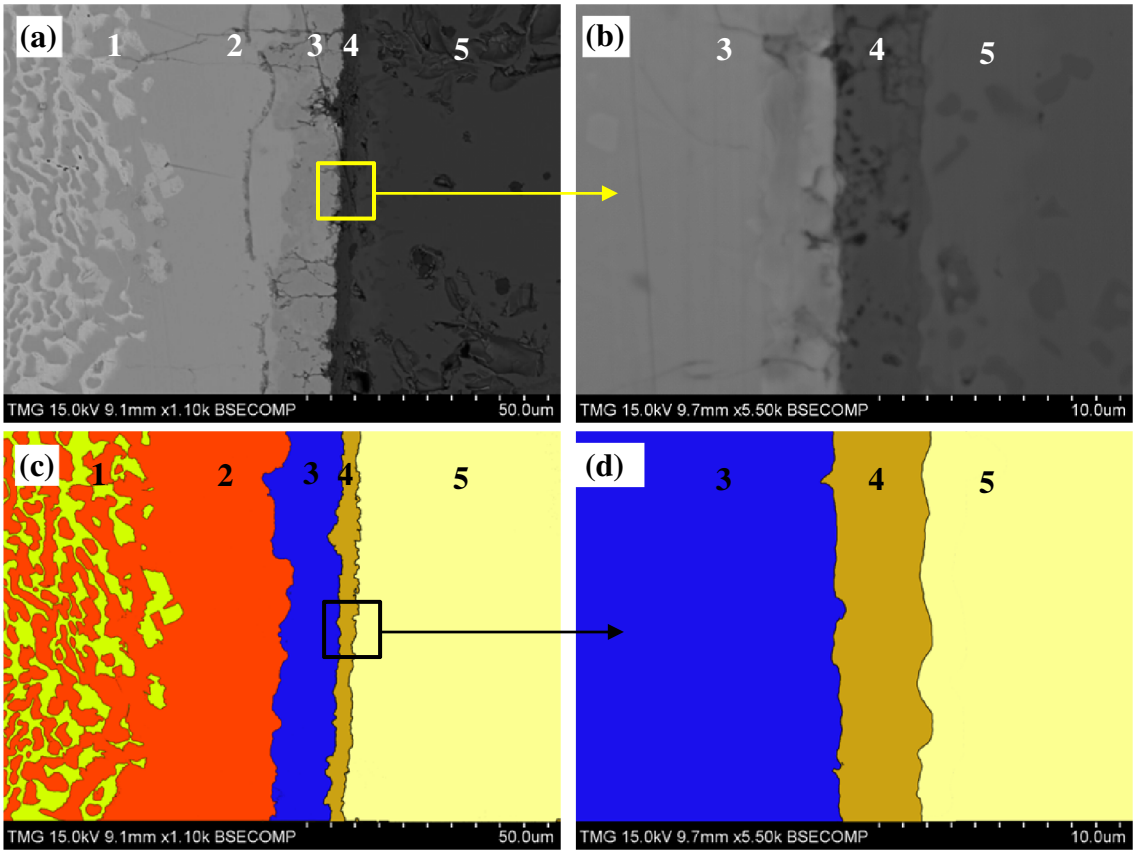

Fig. 6—(*a*, *b*) SEM micrographs of diffusion couple #4; (*c*, *d*) their schematics. The numbers represent the diffusion zones and correspond to those in Fig. 7 and Table V. (For the color interpretation in this figure, it is recommended to refer to the web version of this article).

Table V. Phases Composition Obtained by EDS Spot Analysis and Line-Scan of Diffusion Couple #4

Zone	Description	Composition (at. pct)			Corresponding Phase
		Ce	Mg	Mn	
1	two-phase alloy (end-member)	51.5	48.5	0	CeMg
		94.0	6.0	0	$(\gamma Ce)^{Mg}$
2	single-phase layer	50.0 to 54.8	50.0 to 44.2	0	CeMg
3	single-phase layer	95.3 to 98.7	<2.0 to 3.8	<2.0 to 5.1	$(\gamma Ce)^{Mg,Mn}$
4	single-phase layer	0 to 2.5	0	97.5 to 100	$(\alpha Mn)^{Ce}$
5	pure Mn (end-member)	0	0	100	Mn

also appeared in larger quantity in zone #6 forming the Ce_5Mg_{41} + Mn two-phase region. The presence of Mn in equilibrium with ($CeMg_{12}$) solid solution, in zone #7, confirms the ($CeMg_{12}$) + Mn two-phase region in the ternary diagram in Figure 4.

Although Mn was detected as a pure element in sample #8; traces of fine precipitates of Mn were observed in the ($CeMg_{12}$) solid solution matrix, as shown in Figure 5(b). These precipitates might have resulted from the Mn-supersaturated ($CeMg_{12}$) solid solution, where no more Mn could be dissolved. Thus, according to the phase equilibria in the diffusion couple #3, the diffusion path can be depicted as follows: Ce (end-member) $\rightarrow$ CeMg $\rightarrow$ $CeMg_3$ $\rightarrow$ Ce_5Mg_{41} $\rightarrow$ Mn $\rightarrow$ Ce_5Mg_{41} + Mn $\rightarrow$ ($CeMg_{12}$) + Mn (end-member).

The existence of the thin layer of pure Mn in diffusion couples #1 and 3 gives information about the location of the original interface between the two end-members. For instance, in diffusion couple #1, Mn atoms stopped diffusing at pure Mg end-member; also, no islands of pure Mn were seen on the left side of that thin layer. In diffusion couple #3, the pure Mn layer located in a position where Ce_5Mg_{41} formed on both sides. This leads to the conclusion that Ce_5Mg_{41} layer in zone #4 was formed due to the diffusion of Mg atoms from ($CeMg_{12}$) + Mn end-member toward Ce end-member. Whereas, the Ce_5Mg_{41} layer in zone #6 was formed due

to the diffusion of Ce from Ce end-member toward ($CeMg_{12}$) + Mn end-member.

In order to reveal the phase relations in the Ce-Mg-Mn phase diagram from 50 to 100 at. pct Ce, diffusion couple #4, made from Ce-40 at. pct Mg binary alloy and pure Mn end-members, was prepared. The 60Ce-40Mg (at. pct) binary end-member contains two phases, $(\gamma Ce)^{Mg}$ and CeMg. SEM micrograph of diffusion couple #4 is presented in Figure 6. After annealing at 723 K (450 °C) for 10 days, five diffusion zones were observed. EDS spot analysis was carried out to measure the composition of each zone as listed in Table V. EDS

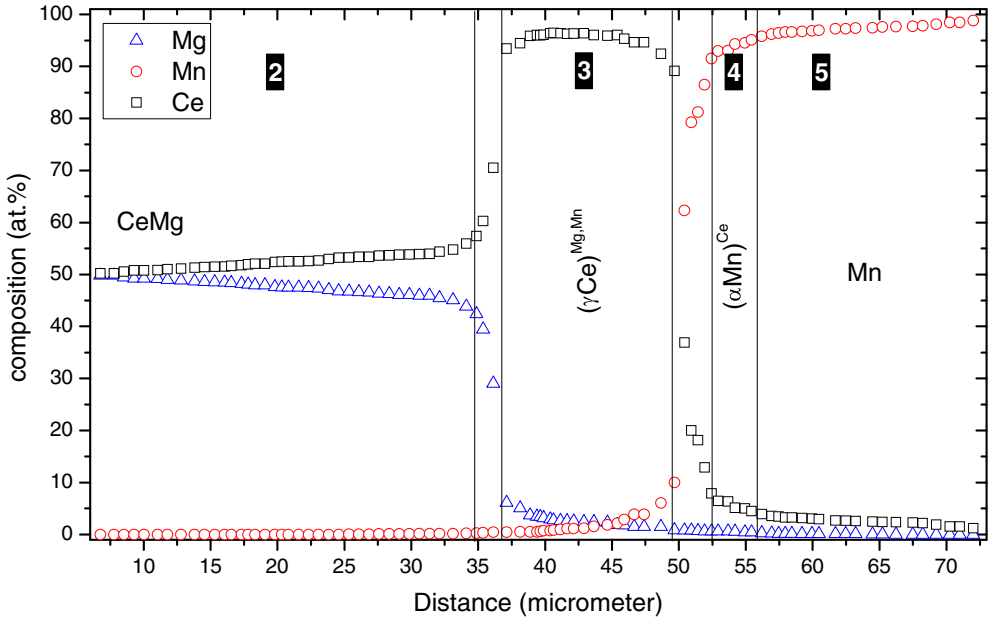

Fig. 7—Composition profile across the diffusion couple #4.

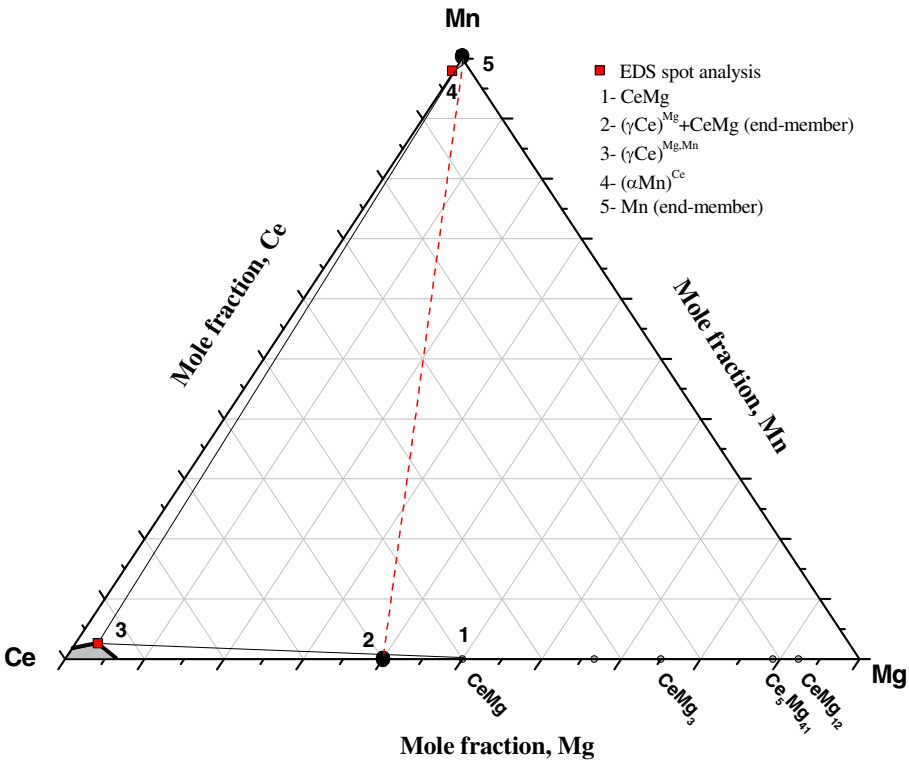

Fig. 8—Phase equilibria depicted from diffusion couple #4.

line-scan across the diffusion zones of diffusion couple #4, shown in Figure 7, was performed to reveal the homogeneity ranges of the binary and ternary solid solutions. According to the composition profile (Figure 7), diffusion zone #2 represents a MgCe layer that formed from the two-phase alloy [$(\gamma Ce)^{Mg}$ and MgCe in zone #1] due to the consumption of Ce, from the $(\gamma Ce)^{Mg}$, during the formation of zones #3 and 4. Diffusion zone #3 represents the $(\gamma Ce)^{Mg,Mn}$ solid solution with 3.8 at. pct Mg and 5.1 at. pct Mn.

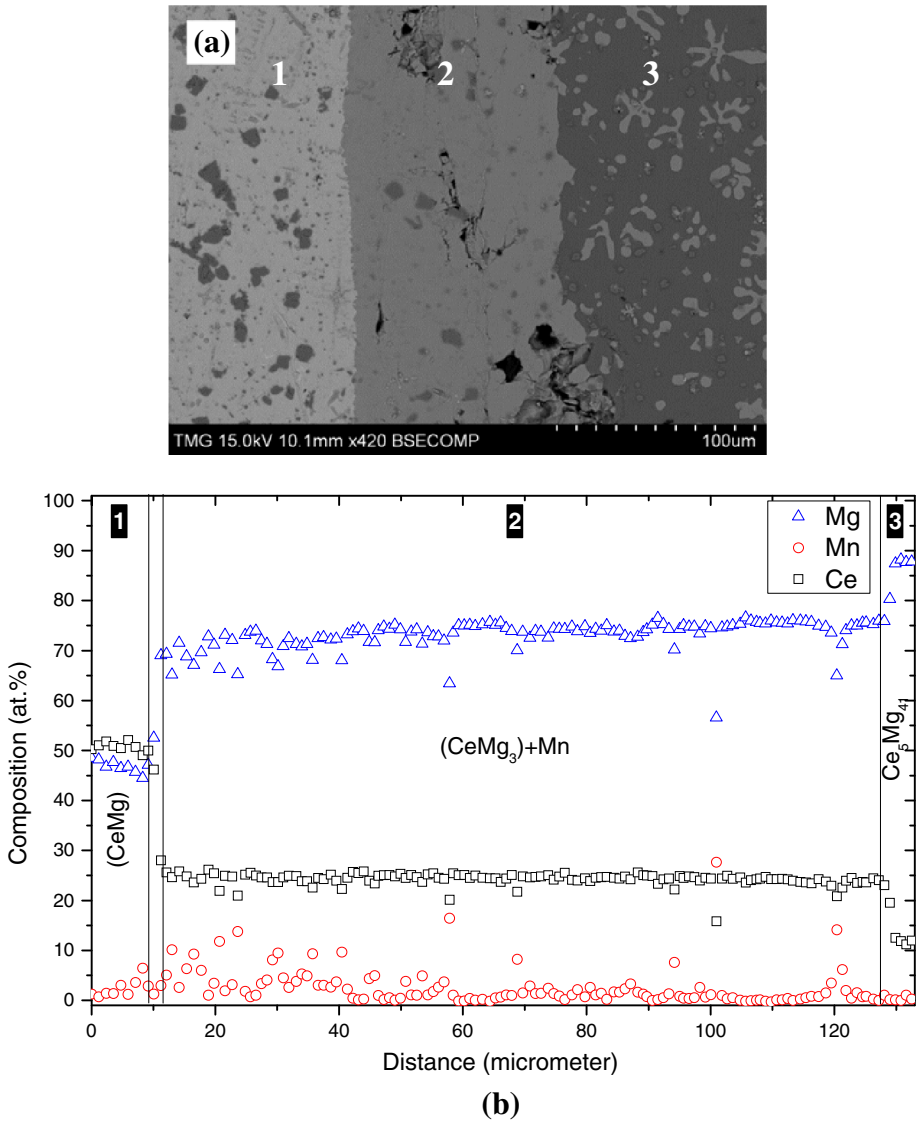

Fig. 9—(*a*) SEM micrograph of diffusion couple #6; (*b*) composition profile across the diffusion couple #6. The numbers represent the diffusion zones and correspond to those in Table VI.

Table VI. Phases Composition Obtained by EDS Spot Analysis and Line-Scan of Diffusion Couple #6

		Composition (at. pct)			
Zone	Description	Ce	Mg	Mn	Corresponding Phase
1	two-phase alloy	50.6	46.4	2.8	(CeMg)
	(end-member)	0	0	100	Mn
2	two-phase layer	25	73.1 to 75	<2.0	$(CeMg_3)$
		0	0	100	Mn
3	three-phase alloy	24.0	75.7	0.3	$(CeMg_3)$
	(end-member)	11.6	88.4	0	Ce_5Mg_{41}
		0	0	100	Mn

Diffusion zone #4 represents the $(\alpha\text{-Mn})^{Ce}$ solid solution which contains 2.5 at. pct Ce. Zone #5 represents the pure Mn end-member.

Mn concentration was found to increase from <2.0 to 6.0 at. pct toward the pure Mn end-member within diffusion zone #3. This increase was attributed to the

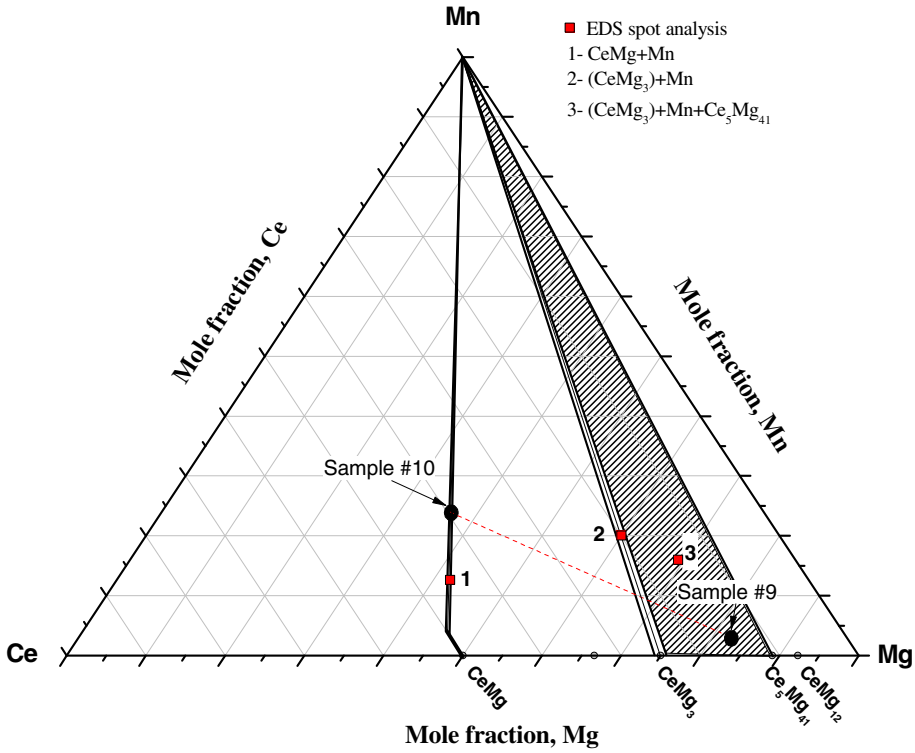

Fig. 10—Phase equilibria depicted from diffusion couple #6.

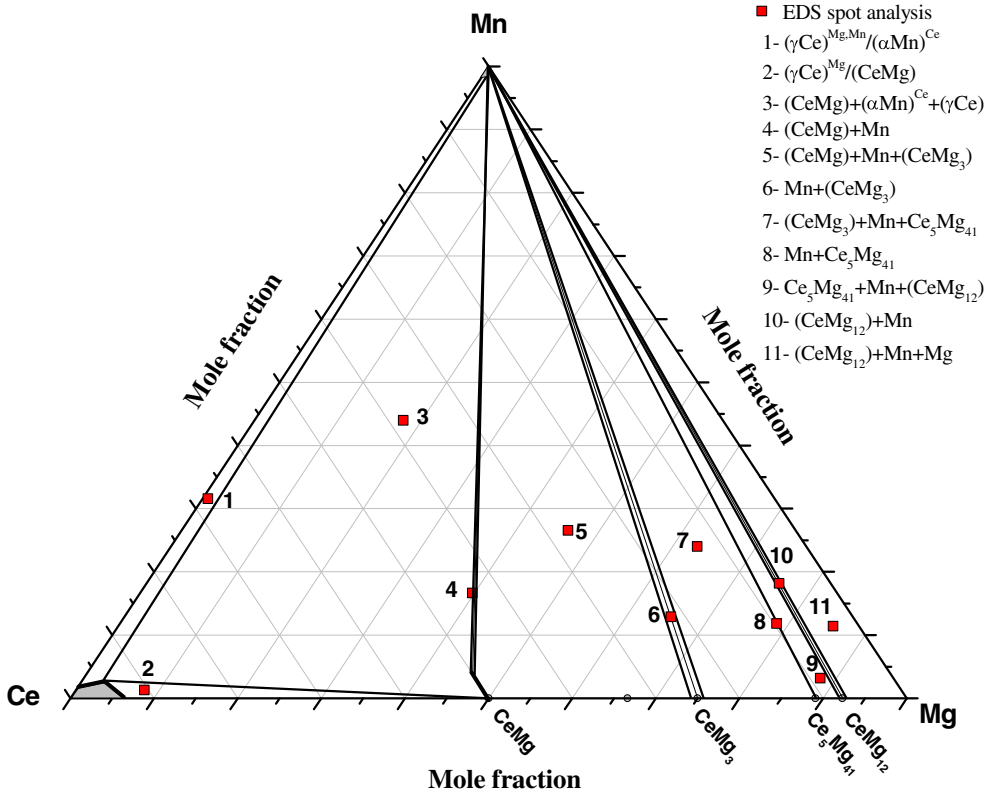

Fig. 11—Phase equilibria determined from diffusion couple studies.

exchange of Mn with the free Ce atoms released from the two-phase end-member. At the same time, the concentration of Mg dropped to <2.0 at. pct at the interface with zone #4, and Ce was stabilized by dissolving small fractions of Mg and Mn to form $(\gamma Ce)^{Mg,Mn}$. Some of the Ce diffused further into Mn end-member to form $(\alpha Mn)^{Ce}$ binary solid solution with 2.5 at. pct Ce. The amounts Ce and Mn in zones #3 and 4 were balanced by the formation of a wide CeMg diffusion layer in zone #2, which relatively contains higher Mg content. Hence, the rule of mass balance in diffusion couple #4 was fulfilled, because the diffusion path intersected the connecting line between the two end-members at least once as shown in Figure 8.

According to the EDS spot analysis and line-scan across the diffusion zones, the phase equilibria depicted from diffusion couple #4 are shown in Figure 8.

Diffusion couple #6 was prepared to investigate the phase relationships in the middle part of the Ce-Mg-Mn phase diagram. The first end-member was made from sample #10 [(CeMg) + Mn] and the second end-member was made from sample #9 [$(CeMg_3)$ + Mn + Ce_5Mg_{41}], as shown in Figure 10. Diffusion couple #6 was annealed at 723 K (450 °C) for 4 days. The SEM micrograph in Figure 9(a) shows the three diffusion zones of diffusion couple #6. These zones are two end-members (zone #1 and zone #3) and one ~116-μm-thick diffusion layer (zone #2). EDS spot analysis was carried out to measure the phase composition of each zone as given in Table VI. EDS line-scan across the diffusion zones was performed to measure the composition profile shown in Figure 9(b). The composition profile shows the Mg/Mn at. exchange at constant composition of Ce in the (CeMg) + Mn phase field (zone #1). The maximum solubility of Mn was measured to be 4.8 at. pct in (CeMg) solid solution.

The line-scan was selected to cut across all possible features in the diffusion zones shown in the micrograph in Figure 9(a). Therefore, the composition profile shows a general concentration trend of each element. The data obtained from the line-scan across zone #2 were noisy (Figure 9(b)). The source of this noise was from the change of average composition measurements in the $(CeMg_3)$ solid solution matrix, where the Mn particles exist. The diffusion path of couple #6 can be depicted as: (CeMg) + Mn (end-member) → $(CeMg_3)$ + Mn → $(CeMg_3)$ + Mn + Ce_5Mg_{41} (end-member). Figure 10 shows a graphical representation of the phase equilibria obtained from this diffusion couple.

The phase relationships, concluded from the phase equilibria obtained from the diffusion couple experiments, are summarized in Figure 11. The numbers 1 to 11 in this figure are used to label the phase regions determined by diffusion couples. The ranges of different solid solutions will be determined more accurately by combining the diffusion couples with the key alloys results.

B. *Key Alloys*

Diffusion couple experiments are not always successful. It is possible to miss some phases due to the slow kinetics of solid–solid reactions.[5,34,35] Therefore, key alloy experiments are designed to verify the experimental results obtained from the diffusion couples. Twelve key alloys were prepared with different compositions to

Table VII. Actual Sample Compositions and Their XRD and EDS Results

	ICP Results (at. pct)					EDS Analysis (at. pct)		
Sample No.	Ce	Mg	Mn	XRD Results	EDS Results	Ce	Mg	Mn
1	54.7	1.8	43.5	Ce	$(\gamma Ce)^{Mg,Mn}$	96.2	2.6	<2.0
				Mn	$(\alpha Mn)^{Ce}$	<2.0	0	98.8
2	52.6	19.8	27.6	(CeMg)	(CeMg)	53.9	43.5	2.6
				Ce	$(\gamma Ce)^{Mg,Mn}$	95.6	3.7	<2.0
				Mn	Mn	0	0	100.0
3*	34.7	38.1	27.2	Mn	Mn	0	0	100.0
4*	40.5	51.0	8.5	(CeMg)	(CeMg)	52.3	44.5	3.2
5*	32.2	53.4	15.4	$(CeMg_3)$	$(CeMg_3)$	25.8	71.3	3.9
6	23.6	72.4	4.0	—	Mn	<1.0	<1.0	98.52
				—	$(CeMg_3)$	23.5	72.8	3.7
7	9.8	82.6	7.6	—	Mn	0	0	100.0
				—	Ce_5Mg_{41}	11.5	88.3	<1.0
8	7.0	87.4	5.6	Mn	Mn	0	0	100
				$CeMg_{12}$	$(CeMg_{12})$	8.0	92.0	0
9	14.5	82.7	2.8	Mn	Mn	0	0	100.0
				Ce_5Mg_{41}	Ce_5Mg_{41}	11.6	88.1	<1.0
				$(CeMg_3)$	$(CeMg_3)$	23.8	75.8	<1.0
10	40.6	35.2	24.2	—	Mn	0	0	100
				—	(CeMg)	50.6	46.4	2.8
11**	43.9	52.5	3.6	$(CeMg_3)$	$(CeMg_3)$	26.4	71.5	2.1
12**	41.2	57.2	1.6	(CeMg)	(CeMg)	52.0	47.2	<1.0

*Samples #3, 4 and 5 fall in the same three-phase region.
**Samples #11 and 12 fall in the same two-phase region.

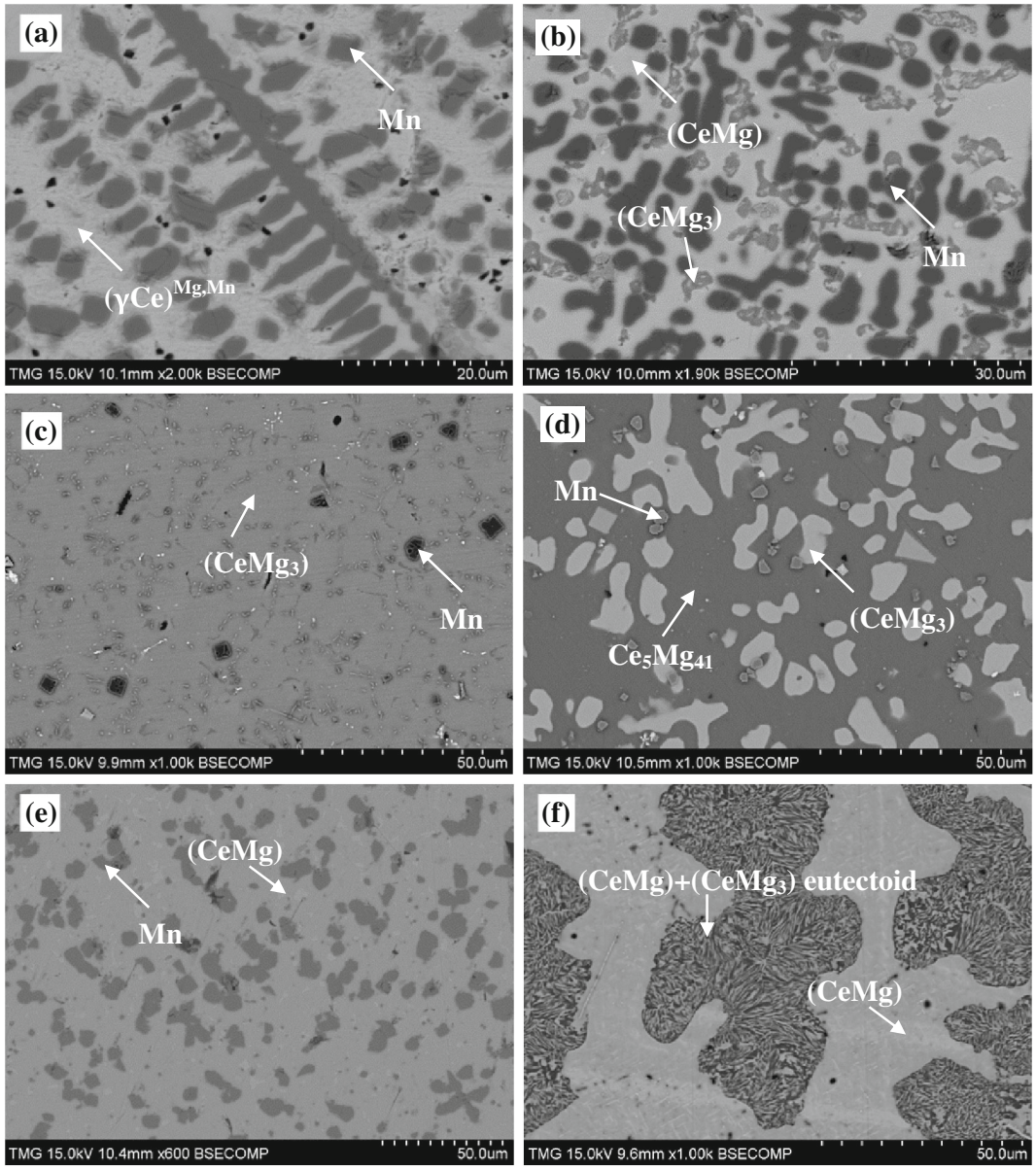

Fig. 12—SEM micrograph of (*a*) sample #1; (*b*) sample #3; (*c*) sample #6; (*d*) sample #9; (*e*) sample #10; and (*f*) sample #11.

verify the phase relationships obtained by the diffusion couples study. Alloys were brought to equilibrium after annealing at 723 K (450 °C) for different periods of time. The actual compositions of the alloys obtained from ICP along with the XRD and EDS results are listed in Table VII. EDS spot analysis was performed on the annealed samples to determine the composition of the observed phases. SEM micrographs for selected alloys are presented in Figure 12. XRD was performed to identify the equilibrated phases and to verify the phase relations obtained from EDS analysis. The XRD patterns of the selected alloys in different regions of the Ce-Mg-Mn system (samples #1, 2, 3, and 9) are shown in Figure 13.

Figure 12(a) shows the SEM micrograph of sample #1, which contains two-phase equilibrium between $(\gamma Ce)^{Mg,Mn}$ ternary solid solution (white phase) and $(\alpha Mn)^{Ce}$ binary solid solution (dark phase). Based on EDS spot analysis, the binary solid solubility of Ce in Mn was measured as <2.0 at. pct Ce; whereas, the ternary solid solution in the Ce-rich corner contains 2.63 at. pct Mg and 1.14 at. pct Mn. Sample #2 was used as an end-member for diffusion couple #1 as shown in Figure 2(d). The three-phase equilibrium was explained in Section IV–A. Figure 12(b) shows the three-phase equilibrium; Mn + (CeMg) + ($CeMg_3$), of sample #3. The binary phase ($CeMg_2$) was not detected in any of the diffusion couples at 723 K (450 °C). Nevertheless, it was observed as metastable phase in sample #3. Two additional alloys (samples #4 and #5) were prepared in the same triangulation to confirm the results obtained from sample #3. Figure 14 shows the two equilibrated phases in sample #12. It was concluded that $CeMg_2$ decomposed eutectoidally to form (CeMg)

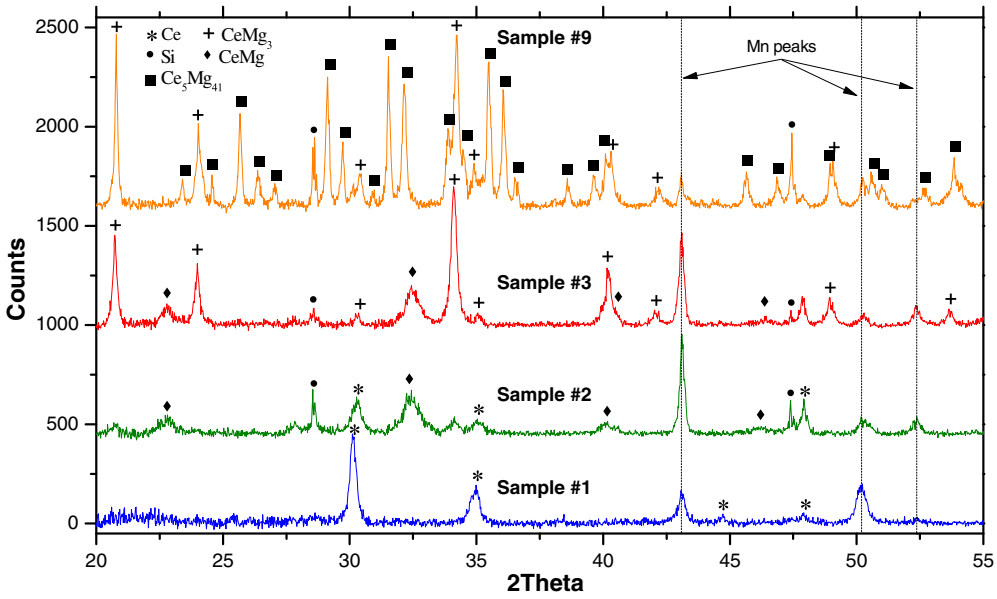

Fig. 13—XRD patterns of samples #1, 2, 3, and 9 selected from different regions of the Ce-Mg-Mn system.

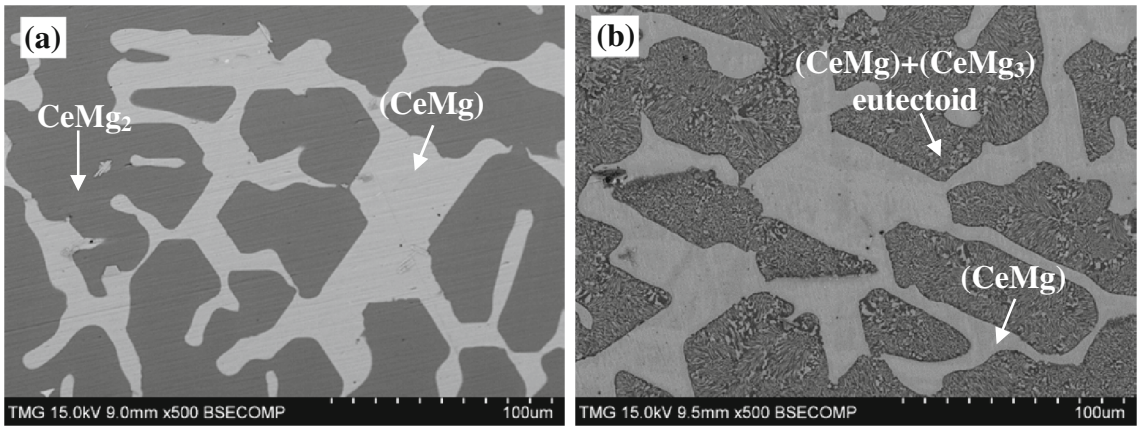

Fig. 14—SEM micrographs of sample #12 (*a*) in the as-cast condition; (*b*) annealed for 27 days.

and ($CeMg_3$) phases. Figure 14 will be discussed in details below. Figure 12(c) shows the two-phase equilibrium between ($CeMg_3$) and Mn in sample #6. The matrix phase contains ($CeMg_3$) ternary solid solution with maximum Mn solubility of 2.5 at. pct. Very fine Mn precipitates were observed in the ($CeMg_3$) matrix indicating Mn supersaturation. Samples #7 and #8 verified the two-phase equilibrium Ce_5Mg_{41} + Mn and ($CeMg_{12}$) + Mn, respectively. The microstructure of sample #8 is shown in Figure 5(b). Three-phase equilibria of sample #9 are shown in Figure 12(d). This alloy was used as an end-member for diffusion couple #6 and discussed in details in Section IV–A. Sample #10, Figure 12(e), was also used in diffusion couple #4; and the phase equilibria were clearly explained in Section IV–A. Samples #11 and #12 were used to confirm the two-phase equilibrium of (CeMg) and ($CeMg_3$). Sample #11, Figure 12(f), shows the eutectoid morphology of (CeMg) + ($CeMg_3$) which resulted from the $CeMg_2$ phase decomposition. The morphologies observed in sample #11 were the same as those of sample #12.

To confirm the results observed by EDS, XRD was used to identify the phases present in the key alloys. The diffusion couples and key alloys showed that Mn is in equilibrium with all phases in the system. This was also confirmed by XRD analysis, where Mn peaks appeared in the diffraction patterns of the analyzed samples, as shown in Figure 13.

As mentioned earlier, the eutectoidal decomposition of $CeMg_2$ into (CeMg) + (Mg_3Nd) was observed in the microstructures of samples #3, 4, 5, 11, and 12. The decomposition mechanism was inferred from Figures 14(a) and (b). Figure 14(a) shows the as-cast microstructure of sample #12. The EDS spot analysis gave the composition of the two phases as $CeMg_2$ and (CeMg). However, from the Ce-Mg binary phase diagram (Figure 1), it can be seen that the thermal

stability range of $CeMg_2$ phase falls between 888 K and 984 K (615 °C and 711 °C); while the annealing was performed at 723 K (450 °C). This means that $CeMg_2$ should not be observed in the equilibrated samples at 723 K (450 °C). Therefore, further annealing was performed for sample #12. Figure 14(b) shows the microstructure of sample #12 after annealing at 723 K (450 °C) for 27 days having typical eutectoid structure.

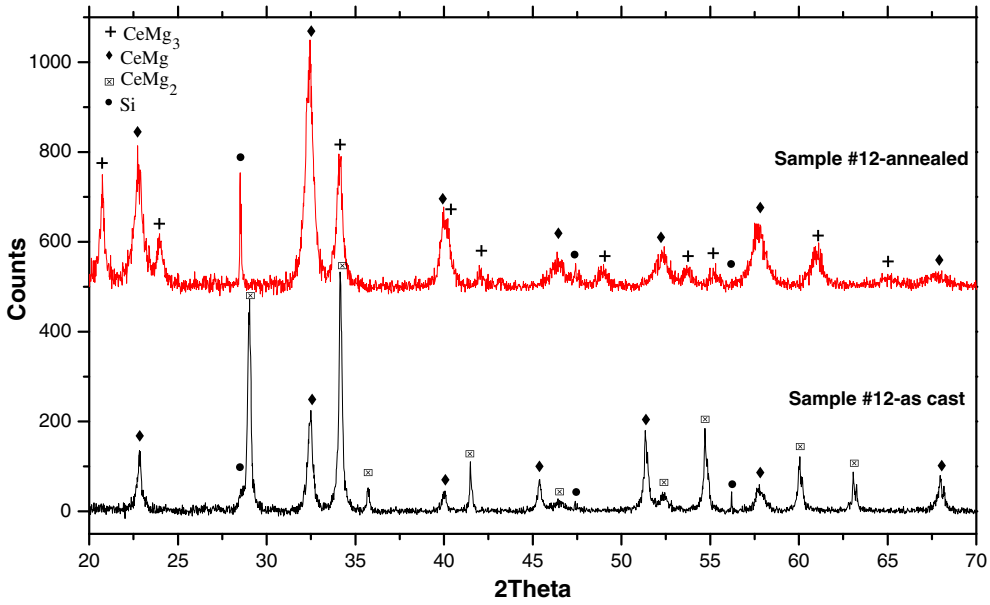

Fig. 15—The as-cast and annealed XRD patterns of sample #12.

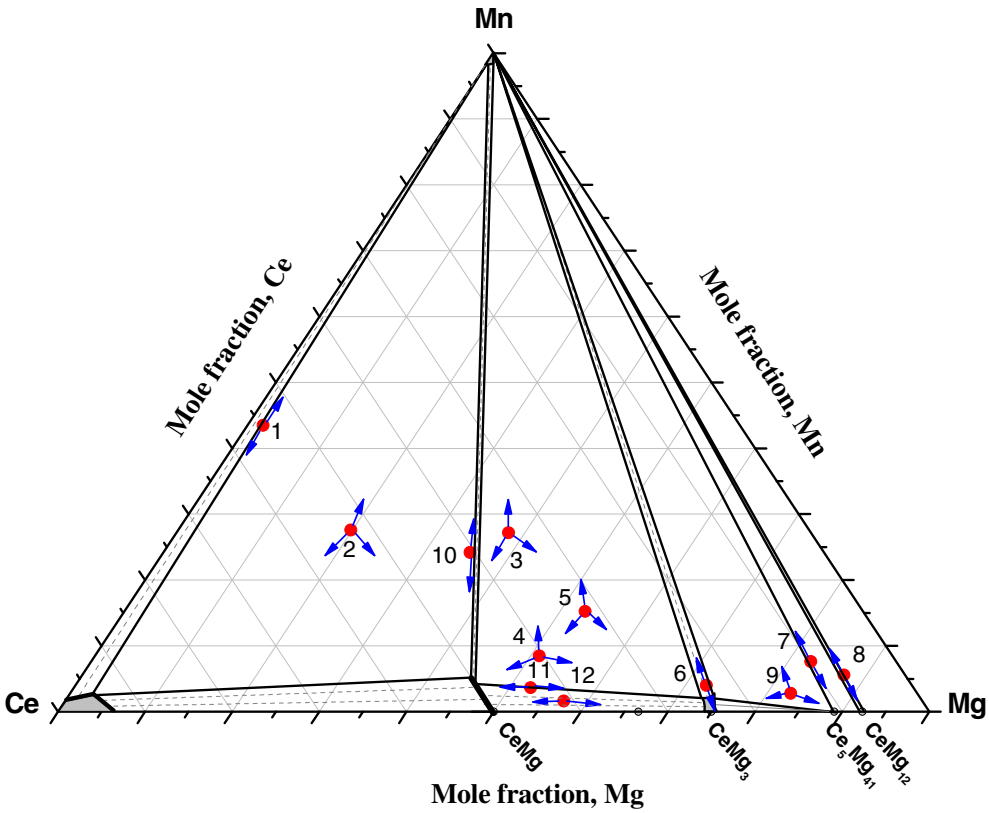

Fig. 16—Phase relationships inferred from phase equilibria and diffusion paths analysis.

Based on the Ce-Mg binary phase diagram (Figure 1), besides the eutectoid structure, it is expected to have the primary solidified (CeMg). Figure 14(b) proves that this is what happened after annealing at 723 K (450 °C) for 27 days. However, due to the fine eutectoid structure, EDS was not accurate enough to obtain the phase composition of its microconstituents. Thus, XRD was carried out to identify the phases present in the as-cast and annealed conditions.

The as-cast and annealed XRD patterns of sample #12 are shown in Figure 15. The XRD pattern of the as-cast sample #12 showed the presence of $CeMg_2$ along with (CeMg). After annealing for 27 days, the XRD pattern of the same sample showed (CeMg) and ($CeMg_3$) only. No peaks of $CeMg_2$ were detected. This ascertains that the eutectoidal decomposition of $CeMg_2$ led to the formation of (CeMg) and ($CeMg_3$). This also provides additional evidence of the presence of the (CeMg) + ($CeMg_3$) phase equilibrium in the Ce-Mg-Mn isothermal section at 723 K (450 °C).

The phase boundaries obtained from the studied key alloys are consistent with those obtained from the diffusion couples technique. These results were combined to establish the Ce-Mg-Mn isothermal section at 723 K (450 °C) as described in the following section.

C. *Ce-Mg-Mn Isothermal Section at 723 K (450 °C)*

The isothermal section of the Ce-Mg-Mn system at 723 K (450 °C), constructed based on the results obtained from the diffusion couples and the equilibrated samples, is shown in Figure 16. The key alloys at the actual composition were shown as solid circles. The arrows indicate the phases obtained from XRD and EDS spot analysis for each alloy.

The (CeMg) + Mn two-phase field was constructed based on the EDS analysis, where Mn showed solid solubility in CeMg up to 5 at. pct. The homogeneity range of the $CeMg_3$ binary solid solution was determined at 723 K (450 °C), in the current work, using diffusion couple #3 as can be seen in Figure 5. The composition profile across the binary diffusion layers, shown in Figure 5(b), showed that the composition of Mg changed from 74.5 to 76.7 at. pct Mg. Accordingly, the binary homogeneity range of ($CeMg_3$) was determined. The ternary solubility of Mn in ($CeMg_3$) was determined as 3.2 at. pct Mn by the diffusion couples and key alloys. Thus, the ($CeMg_3$) + Mn two-phase field was confirmed. The homogeneity range of the ($CeMg_{12}$) binary compound at 723 K (450 °C) is taken from the Ce-Mg binary phase diagram[25] as 0.8 at. pct Mg. This small solubility could not be accurately determined by the EDS in the current work due to the relatively high error limits of Ce (around ±1.5 at. pct).

The Ce-Mg-Mn system shows unique phase relationships, where Mn is in equilibrium with all phases in the system. Since Mn has no tendency to form intermetallic compounds with Ce and Mg, it was always observed as either dissolved in the Ce-Mg compounds or as pure element in all microstructures. Therefore, the phase boundary lines are pointing toward the Mn-rich corner.

V. CONCLUSIONS

The isothermal section of the Ce-Mg-Mn phase diagram at 723 K (450 °C) was constructed for the full composition range. The phase relationships were determined using 6 solid–solid diffusion couples and 12 key alloys. No ternary compounds were detected in the studied system at 723 K (450 °C). Diffusion couple experiments were instrumental in revealing the phase equilibria in this system. However, diffusion couples are not always successful due to the possible missing of some of the phases due their slow kinetics. Therefore, key alloys are essential to complement the diffusion couples. Key alloy experiments were designed to verify the results obtained from the diffusion couples and both results were found to be consistent.

Based on the accepted Ce-Mg binary phase diagram the thermal stability range of $CeMg_2$ phase is between 888 K and 984 K (615 °C and 711 °C), while annealing in this work was performed at 723 K (450 °C). Thus, $CeMg_2$ is not a stable phase in the Ce-Mg-Mn isothermal section at 723 K (450 °C). This was confirmed by SEM/EDS, XRD, and metallographic studies.

Many two-phase regions, composed mainly of Mn and other phase, were observed in the microstructure of each zone. This confirms that Mn was not reacting, and the Mn source was from the ternary alloy end-members. However, the existence of a continuous thin layer of Mn in diffusion couples #1 and 3 indicates that Mn is diffusing.

ACKNOWLEDGMENTS

This research was supported by funding from the Magnesium Strategic Research Network (MagNET). More information on the Network can be found at http://www.MagNET.ubc.ca. The authors would like to acknowledge Mr. Bolarinwa Komolafe from Concordia University for improving the English language.

REFERENCES

1. B. Mordike and T. Ebert: *Mater. Sci. Eng.*, 2001, vol. 302, pp. 37–45.
2. T. Takenaka, Y. Narazaki, N. Uesaka, and M. Kawakami: *Mater. Trans.*, 2008, vol. 49, pp. 1071–76.
3. D. Petrov, M. Mirgalovskaya, I. Strelnikova, and E. Komova: *Baikov IMET RAS*, 1957, vol. 1, pp. 144–47.
4. D. Eliezer, E. Aghion, and F. Froes: *Adv. Perform. Mater.*, 1998, vol. 5, pp. 201–12.
5. A. Kodentsov, G. Bastin, and F. Loo: *J. Alloy. Compd.*, 2001, vol. 320, pp. 207–17.
6. H. Xu, Y. Du, Z. Zhou, and Z. Jin: *Rare Met.*, 2006, vol. 25, pp. 427–30.
7. L. Rolla and A. Iandelli: *Ber. Bunsen-Ges. Phys. Chem (A and B Series)*, 1942, vol. 75, pp. 2091–95.
8. A. Iandelli: *Proc. Natl. Acad. Sci. USA*, 1952, vol. 13, pp. 265–68.
9. B. Thamer: *J. Less-Common Met.*, 1964, vol. 7, pp. 341–46.
10. A. Palenzona and S. Cirafici: *J. Phase Equilib.*, 1996, vol. 17, pp. 53–56.
11. C. Tang, Y. Du, H. Xu, S. Hao, and L. Zhang: *J. Min. Metall.*, 2007, vol. 43, pp. 21–28.
12. C. Tang, Y. Du, L. Zhang, H. Xu, and Z. Zhu: *J. Alloy. Compd.*, 2007, vol. 437, pp. 102–06.

13. Y. Kang, A. Pelton, P. Chartrand, P. Spencer, and C. Fuerst: *J. Phase Equilib. Diff.*, 2007, vol. 28, pp. 342–54.
14. D. Petrov, M. Mirgalovskaya, I. Strelnikova, and E. Komova: *Inst. Mater. Sci. Acad. Sci. USSR*, 1958, vol. 1, pp. 142–43.
15. N. Tiner: *Met. Technol.*, 1945, pp. 1–7.
16. A. Nayeb-Hashemi and J. Clark: *J. Phase Equilib.*, 1985, vol. 6, pp. 160–64.
17. J. Gröbner, D. Mirkovic, M. Ohno, and R. Schmid-Fetzer: *J. Phase Equilib. Diffus.*, 2005, vol. 26, pp. 234–39.
18. M. Asgar-Khan and M. Medraj: *Mater. Trans.*, 2009, vol. 50, pp. 1113–22.
19. X. Zhang, D. Kevorkov, I.-H. Jung, and M. Pekguleryuz: *J. Alloy. Compd.*, 2009, vol. 482, pp. 420–28.
20. D. Wood and E. Cramer: *J. Less-Common Met.*, 1965, vol. 9, pp. 321–37.
21. Q. Johnson and G. Smith: *Acta Crystallogr.*, 1967, vol. 22, pp. 360–65.
22. J. Pahlman and J. Smith: *Metall. Trans. B*, 1972, vol. 3, pp. 2423–32.
23. A. Nayeb-Hashemi and J. Clark: *J. Phase Equilib.*, 1988, vol. 9, pp. 162–72.
24. A. Saccone, D. Macciò, S. Delfino, F. Hayes, and F. Ferro: *J. Therm. Anal. Calorim.*, 2001, vol. 66, pp. 47–57.
25. A. Nayeb-Hashemi and J. Clark: *ASM Handbook, Volume 03—Alloy Phase Diagrams*, ASM International, Materials Park, OH, 1992.
26. X. Zhang, D. Kevorkov, and M. Pekguleryuz: *J. Alloy. Compd.*, 2009, vol. 475, pp. 361–67.
27. H. Okamoto: *J. Phase Equilib. Diffus.*, 2011, vol. 32, pp. 265–66.
28. X. Zhang, D. Kevorkov, and M. Pekguleryuz: *Intermetallics*, 2009, vol. 17, pp. 496–503.
29. X. Zhang, D. Kevorkov, and M. Pekguleryuz: *J. Alloy. Compd.*, 2010, vol. 501, pp. 366–70.
30. P. Villars and L. Calvert: *Pearson's Crystal Data: CD-ROM Software Version 1.3*, 2009.
31. G. Raynor: *Intl. Met. Rev.*, 1977, vol. 22, pp. 65–96.
32. M. Pezat, A. Hbika, and B. Darriet: *Mater. Res. Bull.*, 1980, vol. 15, pp. 139–46.
33. PANalytical Software: *Ver2.2b (2.2.2)*, PANalytical, Almelo, 2006.
34. Md. Mezbahul-Islam and M. Medraj: *J. Alloy Compd.*, 2013, vol. 561, pp. 161–73.
35. Y.N. Zhang, D. Kevorkov, F. Bridier, and M. Medraj: *Sci. Technol. Adv. Mater.*, 2011, vol. 12, pp. 1–13.